ACCSCIENCE PUBLISHING

International Journal of Bioprinting

RESEARCH ARTICLE

Three-dimensional bioprinted personalized repair scaffolds based on CT/MRI fusion imaging after hepatocellular carcinoma resection

Ning Zhou[1], Guanwu Wang[1], Jiaxin Li[2], Wen Liu[1], and Yongzhi Chen[1]*

[1]Department of Hepatobiliary Surgery, Hunan Provincial People's Hospital and the First-Affiliated Hospital of Hunan Normal University, Changsha, Hunan, China

[2]Department of Hepatobiliary Surgery, Northern Jiangsu People's Hospital Affiliated to Yangzhou University, Yangzhou, Jiangsu, China

Abstract

Accurate assessment of residual liver regeneration following hepatocellular carcinoma resection remains a major challenge due to the dynamic nature of the regenerative process and limitations in conventional image-based evaluation. This study develops a three-dimensional (3D) bioprinted personalized repair scaffold based on multimodal fusion of computed tomography (CT) and magnetic resonance imaging (MRI). Multi-temporal CT/MRI images of patients with hepatocellular carcinoma were acquired, registered, and preprocessed using standardization. A dual-channel deep learning network was employed to achieve high-precision liver segmentation and multimodal fusion 3D reconstruction. Using the deformation field from non-rigid registration, the dynamic changes in residual liver volume after surgery were accurately tracked, and the geometry of the resected cavity was extracted to serve as the basis for scaffold design. Subsequently, the internal pore gradient was optimized by combining regeneration rate data. Using a gelatin methacryloyl (GelMA)/hyaluronic acid (HA) composite bio-ink, a repair scaffold with a personalized shape and functional internal structure was manufactured via digital light processing photopolymerization 3D printing. Experiments showed that, in terms of structural fidelity, the GelMA/HA composite scaffold exhibited excellent performance in overall shape fidelity (94.82%) and key structural wall thickness deviation (12.3 μm). Regarding *in vitro* cell compatibility, the relative cell proliferation rate achieved 0.85 ± 0.04 under low-serum conditions. *In vitro* experiments have shown that the scaffold has good cell compatibility and structural stability, providing a theoretical and technical approach for precise repair after liver cancer surgery.

Keywords: Computed tomography/magnetic resonance imaging fusion imaging; Liver cancer resection; Three-dimensional bioprinting; Scaffold design; Gelatin methacryloyl/hyaluronic acid composite materials; Biocompatibility assessment

***Corresponding author:**
Yongzhi Chen
(chenyongzhi@hunnu.edu.cn)

Citation: Zhou N, Wang G, Li J, Liu W, Chen Y. Three-dimensional bioprinted personalized repair scaffolds based on CT/MRI fusion imaging after hepatocellular carcinoma resection. *Int J Bioprint.* 2026;12(3):026140123.
doi: 10.36922/IJB026140123

Received: March 31, 2026

Revised: April 17, 2026

Accepted: April 27, 2026

Published online: May 1, 2026

1. Introduction

Structural and functional reconstruction after hepatocellular carcinoma resection determines the long-term prognosis of patients. Liver regeneration depends on the physical support and biochemical signal guidance of the local microenvironment.[1,2]

Precise anatomical matching prevents complications and constructs an effective regenerative microenvironment.[3] Patient-specific cavities are transformed into bioactive three-dimensional (3D) entities, providing a template for directional growth and mechanical support for new liver tissue.[4,5] The transition from virtual images to functional objects allows surgical correction to evolve from passive filling to dynamic assistance, resulting in improved surgical outcome and quality of life.

Current postoperative management after hepatocellular carcinoma resection remains passive and delayed. In clinical practice, the surgical safety standard uses the remaining liver volume based on preoperative imaging as a fundamental indication to assess surgical safety, and there are no interventions or guidance for the entire postoperative regeneration process.[6,7] Volume variation can be observed in the postoperative imaging follow-up, but the two-dimensional or static 3D data cannot be converted into a dynamic signal to direct tissue repair.[8,9] The nonuniform chambers created by the hepatocellular carcinoma resection are complex geometric shapes and neighboring delicate vascular and bile duct system. Generic filling materials can be compressive, inflammatory, or prevent regeneration.[10,11] Most of the currently available repair materials are based on homogeneous design, and their internal architecture does not mimic the intrinsic natural heterogeneity observed across different liver regions in terms of regenerative potential, blood supply intensity, and metabolic demand.[12,13] The inherent conflict between static filling and dynamic regeneration, therefore, impedes the existing methods for delivering optimal mechanical stability and bioactive microenvironment.[14,15] A gap exists between imaging data and physical repair materials. The models used for preoperative planning cannot be dynamically modified based on actual regenerative progress postoperatively, and the design of repair scaffolds is based on the time of surgery rather than covering the entire regeneration period.[16,17] This gap restricts the accuracy and capability of repair results.

Previous studies on liver regeneration have pursued two different directions. The other is based on biomaterials development, drawing on investigations into the biocompatibility and degradation behavior of hydrogels, porous polymers, and decellularized matrices[18,19], with the intent of offering a substrate for hepatocyte adhesion and culture. Farasati Far *et al.*[20] emphasized that hydrogels, as an innovative local drug delivery system, respond to the tumor microenvironment to achieve controlled release, reduce systemic toxicity, and provide a more precise and safer alternative to traditional chemotherapy for the treatment of hepatocellular carcinoma. Mukherjee *et al.*[21] constructed a nanoporous organic polymer system loaded with upconversion nanoparticles, targeting hepatocellular carcinoma cells and conjugating catalase to relieve hypoxia, overcome tumor multidrug resistance, and enhance the anticancer treatment effect. The other is dedicated to the innovation of medical imaging technology, using computed tomography (CT) or magnetic resonance imaging (MRI) as a single modality for 3D visualization and reconstruction of the liver to assist in surgical planning and risk assessment.[22,23] Jeong *et al.*[24] used deep learning to analyze and enhance MRI images and developed a nomogram model to predict the risk of liver failure after hepatectomy in hepatocellular carcinoma patients, and internal validation showed good predictive accuracy. While the aforementioned studies have made significant progress in their respective fields, the two paths have long been disconnected. Imaging research has stalled at virtual model construction, failing to effectively translate anatomical information into physical entities; materials research lacks individualized anatomical data input, and product design is based on general assumptions, ignoring the significant anatomical differences among patients. Although individual technologies are becoming increasingly mature, a complete closed loop for seamlessly integrating high-fidelity imaging information flow into the manufacture of personalized functional stents has not yet been established, resulting in significant shortcomings in repair solutions regarding precise matching and functional guidance.

Emerging trends in technological convergence are creating new answers to the above issue of fragmentation. The multimodal image fusion technique combines the high spatial resolution of CT and the good soft tissue contrast of MRI to obtain a more detailed 3D liver model[25,26], which provides the basis for accurate extraction of complex geometric features of defect cavities. Deep learning-based image segmentation methods greatly enhance the speed and quality of automatic, precise delineation of the liver contour across multi-temporal images.[27,28] From the perspective of production, recent advances in high-resolution 3D bioprinting methods, such as digital light processing (DLP) printing, enable the fabrication of hydrogel scaffolds with complex external shapes and well-defined internal microstructures.[29,30] Multifunctional bio-inks, such as the typical gelatin methacryloyl (GelMA) and hyaluronic acid (HA), that could enhance cell viability and proliferation inside the printed structures have emerged as promising candidates for tissue engineering applications due to their superior biocompatibility, tunable mechanical properties.[31,32] Prior studies typically employ these sophisticated technologies separately, or at most in combination, to construct in vitro disease models, without

a systemic integration to address the clinical problem of guiding dynamic regeneration following liver resection. The objective is to develop an integrated methodology for multimodal imaging, dynamic regeneration monitoring, gradient scaffold design, and precision biomanufacturing that addresses the imaging- and model-based, static and dynamic process gaps.

This work presents a novel technical scheme for accurate repair following liver cancer resection. The essence is the close coupling of multi-temporal CT/MRI fusion imaging, deformation-field-based dynamic regeneration quantitative analysis of the residual liver, and DLP high-precision 3D bioprinting technology. These fused images accurately reproduce the personalized shapes of postoperative cavities to explore regeneration dynamics information embedded in multi-temporal images. On this basis, an internal biomimetic structure with spatially graded porosity is proposed, and the scaffold's physical properties meet local regeneration demands. The GelMA/HA composite bio-ink is employed to provide superior biocompatibility and cell responsiveness of the scaffold. This strategy overcomes the limitations of conventional static filling and develops a smart repair carrier that dynamically responds to and possibly steers the liver. A systematic ex vivo biocompatibility assessment of the synthesized scaffold confirms its feasibility and superiority as a personalized repair strategy for the liver, with potential applications in liver resection, offering theoretical and technical support for further clinical translation.

2. Computed tomography/magnetic resonance imaging fusion-driven personalized scaffold design

Figure 1 systematically illustrates the liver repair scaffold design based on multimodal imaging and 3D printing. Multi-temporal CT/MRI images were registered, fused, and annotated by experts to complete data preprocessing. A dual-channel deep learning network was used to achieve high-precision liver segmentation and 3D reconstruction, extracting personalized anatomical models. The dynamic regeneration process of the residual liver was tracked using non-rigid registration; the geometry of the resected cavity was extracted; and a gradient pore structure was designed based on the regeneration rate. Personalized scaffolds were 3D printed using GelMA/HA bio-inks for DLP[33,34], and their biocompatibility was evaluated using *in vitro* experiments. This architecture realizes a complete technical closed loop from image data to functionalized prostheses.

2.1. Multi-temporal computed tomography/magnetic resonance imaging image acquisition and preprocessing

This study simulates a clinical liver regeneration monitoring scenario after hepatectomy using publicly available multimodal liver imaging datasets LiTS2017 (including preoperative/postoperative CT scans of hepatocellular carcinoma patients) and CHAOS (including T2-weighted MRI). The CT and MRI data used correspond to virtual preoperative and multiple postoperative time points, respectively, to construct a dynamic regeneration analysis workflow. CT used a multi-phase enhancement scheme to acquire portal venous phase data, and MRI acquired axial T2-weighted sequences.[35,36] Raw Digital Imaging and Communications in Medicine data were imported into the image workstation and uniformly converted to Neuroimaging Informatics Technology Initiative (NIfTI) format. All data were spatially resampled to an isotropic voxel resolution. The resampling process was based on a trilinear interpolation function to construct a continuous intensity field; the expression is shown in **Equation 1**:

$$I'(x,y,z)=\sum_{i=0}^{1}\sum_{j=0}^{1}\sum_{k=0}^{1}w_{ijk}I(x_i,y_j,z_k) \quad (1)$$

where $I'(x,y,z)$ represents the gray value at the target coordinates (x,y,z) after resampling; $I(x_i,y_j,z_k)$ represents the gray value of the eight vertices in the original voxel neighborhood; w_{ijk} is the interpolation weight coefficient related to spatial distance. This step unifies the spatial resolution differences across devices and scanning protocols, ensuring consistency of multi-temporal data at the voxel level. For MRI images exhibiting intensity non-uniformity, the N4 field correction algorithm is applied. The image intensity model is expressed as **Equation 2**:

$$I_{\text{obs}}(x)=I_{\text{true}}(x)\cdot B(x)+n(x) \quad (2)$$

where $I_{\text{obs}}(x)$ is the observed intensity; $I_{\text{true}}(x)$ is the true tissue signal; $B(x)$ is the low-frequency field distribution function; $n(x)$ is the noise term. N4 is applied in a way similar to the N3 algorithm, fitting the B-spline parameterization in the log domain to the data and energy in a number of iterations. The corrected image is then subjected to intensity normalization, which normalizes the gray-level range by applying a linear scaling operation and removes temporal and intensity variations.

The MRI and CT images from the same subject at the same time point are co-registered using a mutual-

information-based affine registration approach. The objective function for registration optimization is based on mutual information (**Equation 3**):

$$MI(A,B)=\sum_a\sum_b p_{AB}(a,b)\log\frac{p_{AB}(a,b)}{p_A(a)\,p_B(b)} \tag{3}$$

where $MI(A,B)$ represents the mutual information between images A and B; $p_{AB}(a,b)$ is the joint probability distribution function; $p_A(a)$ and $p_B(b)$ are the marginal probability distributions, respectively. Rotation, translation, scaling, and shearing are the components of the affine transformation matrix. The best parameter combination is sought using a gradient descent approach to maximize cross-modal grey-level statistical correlation and spatial consistency of anatomical structures. This is followed by the alignment accuracy confirmed through visual overlay and error-field analysis.

The registered data were imported into ITK-SNAP software (version 3.8.0, University of Pennsylvania, USA) for manual fine annotation. Two physicians with imaging diagnostic qualifications independently delineated the overall liver contour and tumor region, constructing a 3D mask using a layer-by-layer axial-slice depiction method. Discrepancies in the region were revised through negotiation to form a unified annotation result. The annotation file was saved as a binary mask, and a spatial index was established for the corresponding image. Finally, a standardized labeled dataset covering all time points was generated, providing a consistent reference benchmark for subsequent model training and validation.

Figure 2 shows four 3D histogram subplots. The horizontal axis represents spatial orientation; the vertical axis represents time points; the vertical height represents voxel resolution (unit: mm^3). Figure 2A shows the CT resolution data before resampling, specifically: Pre-op (0.8, 0.8, 1.5), Week 1 (0.9, 0.9, 1.4), Week 2 (0.7, 0.7, 1.6), Month 1 (0.85, 0.85, 1.45). The Z-axis resolution is significantly higher than the XY-plane resolution, and there are slight fluctuations at each time point. Figure 2B shows the MRI resolution data before resampling: Pre-op (1.2, 1.2, 3.0), Week 1 (1.3, 1.3, 3.2), Week 2 (1.1, 1.1, 2.8), Month 1 (1.25, 1.25, 3.1). The Z-axis resolution is significantly lower than that of CT, and it varies over time. Figure 2C and 2D show the data after resampling, with all time points uniformly set to (1.0, 1.0, 1.0). The cylinder heights are completely consistent, indicating that voxel isotropic standardization has been completed. The data changes illustrate that before resampling, CT and MRI show significant differences in Z-axis slice thickness, with inconsistencies over time. After resampling, the spatial resolution at each time point is uniform, eliminating differences in longitudinal sampling intervals and providing a stable spatial basis for cross-phase analysis and registration.

2.2. Multimodal liver segmentation and fusion reconstruction based on deep learning

A dual-channel encoder-shared decoder[37,38] convolutional neural network architecture was constructed. Registered CT and MRI 3D image blocks were input into independent encoding paths. Each encoder consisted of multiple layers of 3D convolution, batch normalization, and nonlinear activation units stacked together. The convolution operation is expressed as **Equation 4**:

$$F_I=\sigma(W_I * F_{I-1}+b_I) \tag{4}$$

where F_I represents the output feature map of the layer I; F_{I-1} is the feature map of the previous layer; W_I is the convolution kernel weight parameter; b_I is the bias term. $*$ represents the 3D convolution operation, and σ is the nonlinear activation function. The independent encoding paths preserved the original texture and intensity distribution differences across modalities, extracted spatial context information layer by layer, and completed feature compression.

The decoding stage shares the decoder with the multi-level fusion mode, which follows the channel-wise splicing and group-wise upsampling step by step. A concatenation result of known: the fused feature map, is defined as follows (**Equation 5**):

$$F_{fusion}=\phi\left(concat\left(F_I^{CT},F_I^{MRI}\right)\right) \tag{5}$$

where F_I^{CT} and F_I^{MRI} are the CT and MRI encoded features at the same level, respectively. $concat$ is the operation of concatenating in the channel dimension, and ϕ is the convolution mapping proceeding. This operation combines the high spatial resolution of the MR images with soft tissue contrast, resulting in more consistent boundary recognition. The network ends with a Sigmoid function to produce a probability map, which is then thresholded to obtain a 3D liver mask. During the training, parameters are updated by the Dice loss function, which is defined as **Equation 6**:

$$L_{Dice}=1-\frac{2\sum_i p_i g_i}{\sum_i p_i^2+\sum_i g_i^2} \tag{6}$$

where p_i represents the predicted probability value of the i-th voxel, and g_i represents the corresponding

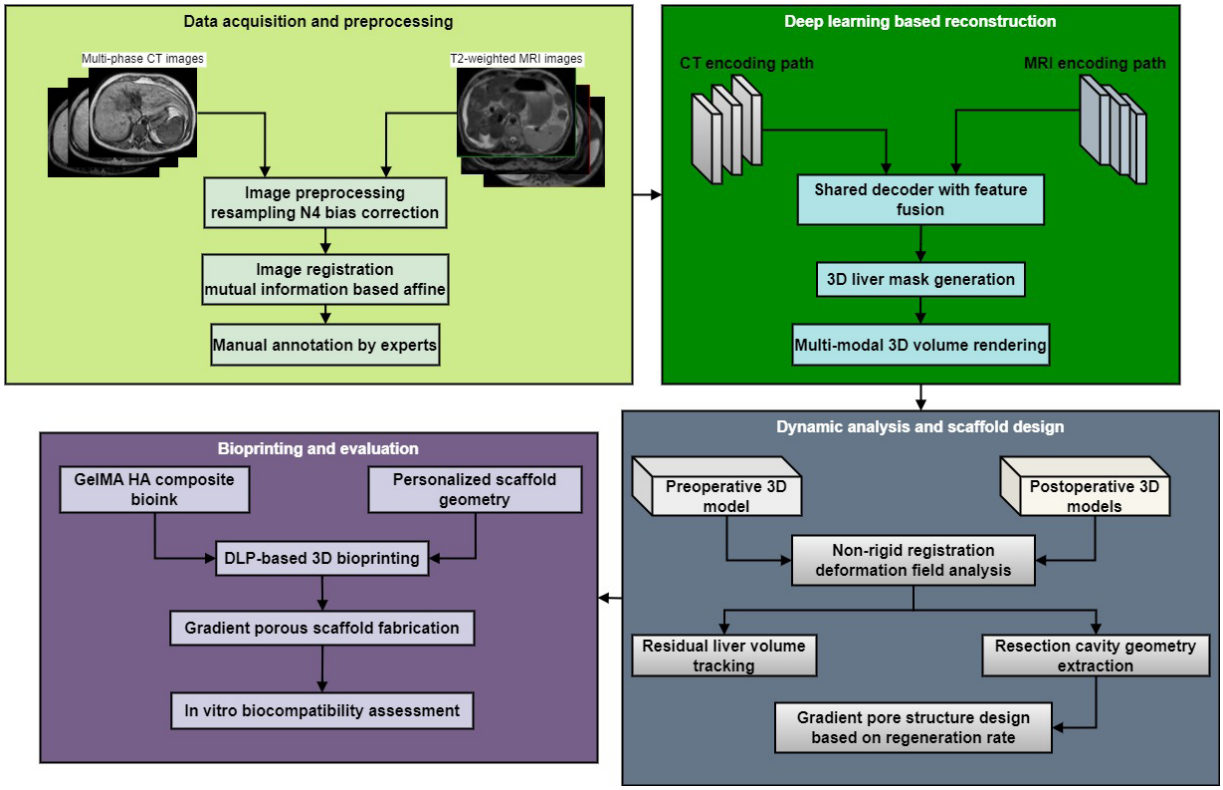

Figure 1. Design of a liver repair scaffold based on multimodal imaging and three-dimensional printing
Abbreviations: CT: Computed tomography.

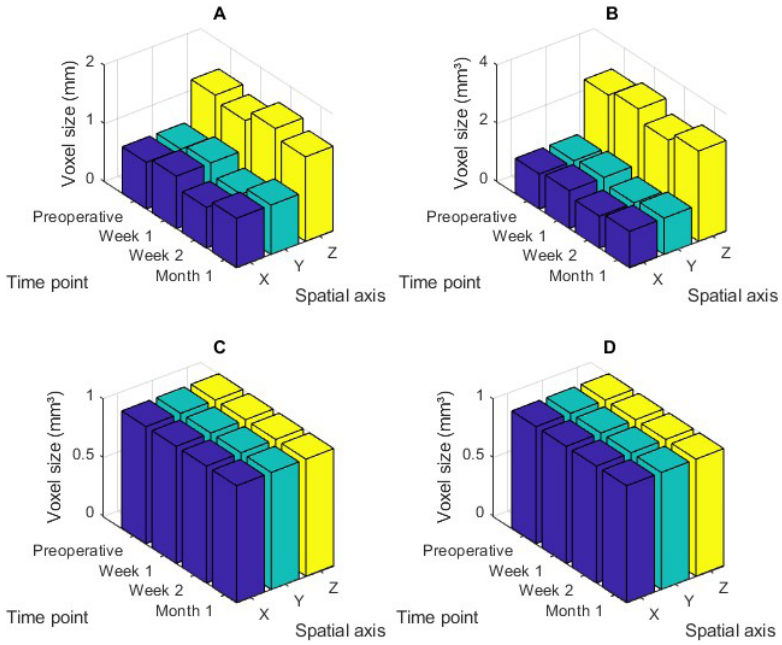

Figure 2. Resampling consistency and spatial resolution normalization. (A) Computed tomography (CT) resolution before resampling. (B) Magnetic resonance imaging (MRI) resolution before resampling. (C) CT Resolution after isotropic resampling. (D) MRI Resolution after isotropic resampling.

true label value. This loss function quantifies the similarity between the predicted region and the labeled region, thereby reducing the effect of class imbalance on the gradient computation of labels.

The generated 3D mask was then applied to the original CT data: the liver parenchyma was preserved, and the signal from the surrounding tissue was zeroed stage-wise via logical filtering along the voxel axes. The cropped data exhibited spatial relationships with the grayscale MRI field, forming a paired dataset. The experience process was implemented using a ray casting algorithm. For each pixel on the observation plane, a sampling ray was fired, and the voxel intensities were integrated and accumulated along the ray path. The color synthesis formula is written as **Equation 7**:

$$C = \int_0^D T(s)\tau(s)c(s)ds \tag{7}$$

where C is the final pixel color value; D is the propagation distance of the ray in the volume data; $T(s)$ is the transmission function; $\tau(s)$ is the voxel opacity function; $c(s)$ is the color mapping value at the sampling position; S is the spatial parameter along the ray. The transfer function was recursively updated based on the accumulated opacity, which enabled the retention of high-depth occlusion information and attenuation of interference from non-focal regions. CT data had well-defined anatomical boundaries, and the MRI grayscale was used for color mapping to better differentiate the soft tissue layers. The complete generated 3D model, which revealed the spatial relationship between the liver's shape and the postoperative deficient region, had a smooth, uninterrupted surface with no visual artifacts or disruptions, and met the precision requirement for subsequent structural design.

The two-dimensional anatomical coordinates in Figure 3A illustrate the reconstructed volume data of discrete voxels. The corresponding voxel's grayscale intensity (vertical height) indicates the spatial distributed pattern for each modality signal (i.e., different types of modal signals) at 3D volumes rendering from a different perspective of 3D visual impression.

In Figure 3A, a steep boundary and continuous contour intensity distribution exist; the grayscale variation is mainly within the outside area, and the intensity variation in the inside area is relatively much smaller. It is the importance of high-resolution imaging data in volume rendering that gives rise to this characteristic. Sharp grayscale gradients at the boundaries and small spatial extent of these gradients further confirm accurate localization of the structural information. The almost homogenous appearance of the internal intensity distribution suggests that a single structural signal is not effective in representing variability within the soft tissue, and the voxel intensity field contains richer geometrical contour information than the single scalar field of a voxel.

Figure 3B presents a smoothly undulating intensity surface; the grayscale variation becomes milder in the bound region, and the intensity in the inner region fluctuates continuously. The spatial distribution of intensity has a multi-scale and layered, gradually changing pattern, implying that the contrast of the soft tissue signal dominates in volume rendering. The edge blurring effect is due to the amplification of low-frequency components in the signal as it propagates in space, resulting in an increase in the grayscale transition width and a relative loss of edge localization precision. The enhanced magnitude of internal grayscale fluctuations corresponds to increased signal representation of contrasts across tissue types.

Figure 3C shows a fused image that simultaneously displays a crisp external contour and a well-layered internal structure. The boundary regions have a large grayscale gradient, and the intensity and texture in the inner region vary clearly in space. The fusion result has a layered high-intensity distribution, revealing the accumulation of high-frequency structural information and medium- and low-frequency contrast information. The spatial intensity surface has clear anatomical interfaces and enhances the expression of within-soft-tissue heterogeneity. The full-intensity field is well-smoothed, with no obvious jumps or tears, indicating that multimodal features are well fused during the volume rendering procedure and achieve the simultaneous benefits of structural fidelity and tissue-specific expression.

2.3. Dynamic regeneration volume tracking and defect model generation of residual liver

Spatial registration was performed between the 3D liver models at different postoperative time points and the preoperative model. An intensity-based Demons non-rigid registration algorithm was used to estimate deformations. This method refined the displacement field iteratively within a continuous iterative framework. The incremental displacement of a single iteration is expressed as **Equation 8**:

$$\Delta u = \frac{(I_f I_m)\nabla I_f}{\|\nabla I_f\|^2 + (I_f I_m)^2} \tag{8}$$

where Δu represents the displacement increment vector of the current iteration; I_f is the grayscale field of the fixed image; I_m is the grayscale field of the moving image; ∇I_f is the idle gradient of the fixed image; $\|\nabla I_f\|^2$ is the

squared magnitude of the gradient. The displacement field is constrained by Gaussian smoothing to suppress local discontinuous deformation. The Demons algorithm was configured with a maximum iteration limit of 300 iterations or early termination when the displacement field change was less than 1×10^{-4} voxels. A Gaussian smoothing kernel with a standard deviation of 1.5 voxels was used to enforce spatial continuity of the displacement field and prevent non-physiological folding. After multiple iterations, a stable 3D deformation vector field was obtained, achieving accurate voxel-level alignment of liver structures across different time points. The registration results were tested for consistency using a Jacobian determinant distribution to exclude non-physiological topologies.

After spatial alignment, voxel-by-voxel volume statistics were computed for the distance between the liver masks at each time point. The total volume of the residual liver was calculated as shown in **Equation 9**:

$$V_t = \sum_{i=1}^{N} m_i \cdot v \tag{9}$$

where V_t represents the total volume of the residual liver at the time point t ; m_i is the binary mask label of the i -th voxel; v is the volume of a single voxel; N is the total number of voxels within the mask. The immediate volume after surgery was used as the baseline volume to construct the regeneration rate function (**Equation 10**):

$$R_t = \frac{v_t - v_0}{v_0} \tag{10}$$

where R_t represents the regeneration rate at the time point t , and v_0 is the immediate liver volume after surgery. The regeneration rates of each phase were arranged in chronological order to form a continuous dynamic change curve. Combined with the deformation vector field, the local volume expansion ratio was further calculated to obtain a spatial distribution feature map, revealing differences in regeneration across regions.

In the immediate postoperative 3D model, the cavity region formed by tumor resection was separated from the intact liver model using Boolean operations. The cavity boundaries were extracted, and the continuous triangular mesh model was constructed using the Marching Cubes algorithm. Laplacian smoothing was applied to the surface mesh to remove discretization noise and preserve the model's smooth geometric shape. The local concave and convex features can be measured using the boundary curvature distributions, which makes the model preserve the local true spatial relations of the sub-region near the blood vessel. The resulting cavity solid model was converted to a standard 3D format file, which was used as the external geometric template for the stent.

A coordinate transformation was defined between the cavity model and the distribution map in the space of the regeneration rate. The cavity interior was segmented into a number of gradient segments based on the volume growth rates of different areas. The porosity parameters in each segment were associated with the corresponding regeneration rate via a function mapping; high-regeneration-rate regions were assigned a relatively dense structure, while low-regeneration-rate regions were assigned a relatively loose structure, resulting in a continuous pore-gradient distribution. The scaffold porosity ϕ is mapped to the local regeneration rate r via a piecewise linear function defined as **Equation 11**:

$$\phi(r) = \begin{cases} 0.75, & r < 0.1 \\ 0.75 - 1.5(r - 0.1), & 0.1 \le r \le 0.4 \\ 0.30, & r > 0.4 \end{cases} \tag{11}$$

Here, r denotes the normalized regeneration rate (ranging from 0 to 1). This mapping yields high porosity in poorly regenerating regions (to facilitate nutrient diffusion and cell infiltration) and lower porosity in highly regenerative zones (to provide mechanical support). This design is grounded in pilot observations: regions with regeneration rates below 10% typically reside in areas of weak perfusion and benefit from an open architecture, whereas regions exceeding 40% regeneration require denser microstructures to maintain structural integrity during active tissue ingrowth.

The pore network was created using a regular grid, with pore size and the support beam diameter controlled by parametric modeling software to balance internal mechanical support and cell migration through the channel. The 3D stent model was stored after verifying the geometric consistency of the generated model, providing correct input data for the manufacturing step.

2.4. Three-dimensional bioprinting of scaffolds based on gelatin methacryloyl/hyaluronic acid composite materials

Methacrylamide gelatin and hyaluronic acid were weighed as the raw material and dissolved in the sterile phosphate buffer. The solution was stirred magnetically at a constant temperature until a uniform result was obtained. A photoinitiator was added and stirred in the dark to form a photosensitive composite bio-ink. The GelMA used had a methacryloylation degree of 85% (as determined using

^{1}H nuclear magnetic resonance [AVANCE III 400 MHz, Bruker Corporation, Germany]), and the HA modified with methacrylic anhydride exhibited a substitution degree of 40%. After photoligation, the gel maintained a mass retention rate of 68% in PBS at 37 °C for 14 days, indicating that its degradation rate matched the regeneration cycle of liver tissue. The material fraction was filtered using a rheology test. A dynamic shear rate sweep was conducted on a rotational rheometer (MCR 302, Anton Paar GmbH, Austria), and the shear stress versus shear rate was traced. The apparent viscosity of the system is given by **Equation 12**:

$$\eta(\dot{\gamma}) = \frac{\tau}{\gamma} \tag{12}$$

where $\eta(\dot{\gamma})$ represents the apparent viscosity at the shear rate $\dot{\gamma}$, and τ is the corresponding shear stress. From the analysis of the shear-thinning behavior and the viscosity plateau region, it can be concluded that the material exhibits steady flow prior to irradiation. Further oscillation frequency scans were performed to obtain the storage modulus and loss modulus curves, which describe the structural integrity of the prepolymer. The storage modulus and loss modulus are defined as **Equations 13 and 14**:

$$G' = \frac{\sigma_0}{\gamma_0}\cos\delta \tag{13}$$

$$G'' = \frac{\sigma_0}{\gamma_0}\sin\delta \tag{14}$$

where G' is the storage modulus; G" is the loss modulus; σ_0 is the stress amplitude; γ_0 is the strain amplitude; δ is the phase difference. The material maintains a viscoelastic balance in the low-frequency region, and after exuding and curing, it develops into a stable 3D network structure. The finished 3D support model was imported into the slicing software Creation Workshop (version 2.6.7, EnvisionTEC, USA), and the layer thickness parameter and the exposure time matrix were set. Layer-by-layer projection images were generated using the software, based on the model's geometric contour and the light-field distribution associated with the internal porous network. A layer-by-layer exposure strategy was employed in path planning to prevent over-curing of consecutive regions and thus prevent pore closure. The printing was performed in a closed chamber with constant ambient temperature and humidity. A DLP device utilized a digital micromirror array to shape ultraviolet (UV) light patterns, layer by layer, on the bottom of the resin vat. During the photopolymerization reaction, the free radical concentration varies according to **Equation 15**:

$$\frac{d[M]}{dt} = -kp[M][R^{\bullet}] \tag{15}$$

where $[M]$ is the monomer concentration; $[R^{\bullet}]$ is the free radical concentration; k_p is the chain growth rate constant. In the exposed area, the monomer gradually transformed into a cross-linked polymer network, while the unexposed area remained liquid. Once each layer was cured, the platform moved a predefined increment vertically to begin the next layer-exposure cycle, continuing until the entire volume was constructed. The size of the internal pores and the dimensions of the support beams were accurately tailored using projection profiles to match the porous network to the external contour. The key process parameters for DLP printing were as follows: UV light source wavelength of 405 nm, light intensity of 12.5 mW/cm^2; single-layer exposure time of 8 s; platform peeling distance set at 50 μm, and peeling speed of 100 μm/s. These parameters were optimized through preliminary experiments to ensure curing integrity while avoiding pore closure caused by excessive cross-linking.

Following printing, the molded scaffold was released and soaked in sterile phosphate buffer to wash away unreacted monomers and residual photoinitiators. The soaking process led to additional hydration and chain reorganization within the network, thereby enhancing structural integrity. The buffer was replaced until the eluent was colorless. The treated scaffold was kept in sterile conditions for later performance testing. To evaluate cleaning efficacy, UV–visible spectrophotometry (NanoDrop One, Thermo Fisher Scientific, USA) was used in the preliminary experiment to measure the absorbance of the final eluate at 365 nm, confirming that it was below the detection limit (<0.01). This indicates that the photoinitiator has been largely removed, with residual amounts insufficient to cause significant cytotoxicity. Throughout the entire fabrication process, a uniform light dose and material ratio were maintained to ensure the geometric fidelity of the scaffold and the integrity of its inner microporous structure.

3. Comprehensive performance evaluation of personalized repair scaffolds

3.1. Experimental data and setup

As core data, this study was based on publicly available multimodal liver imaging datasets, LiTS2017 (https://github.com/assassint2017/MICCAI-LITS2017) and

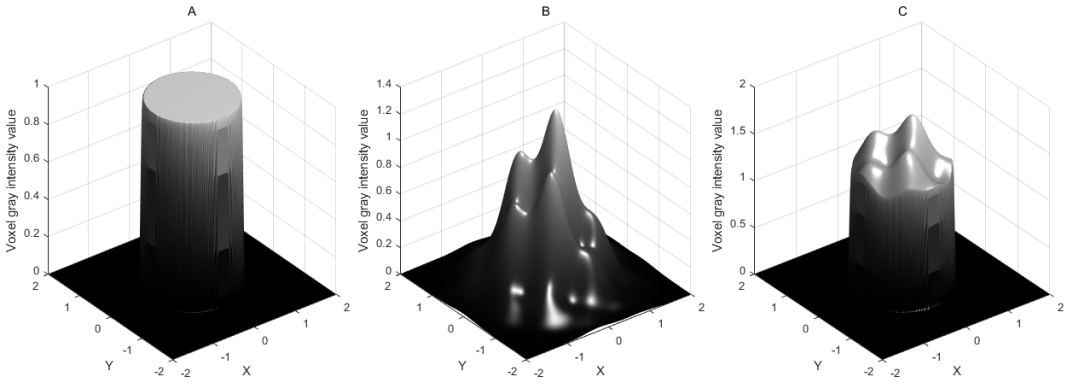

Figure 3. Multimodal fusion three-dimensional volume rendering. (A) High spatial resolution computed tomography. (B) Soft tissue contrast of magnetic resonance imaging. (C) Fused volume rendering.

CHAOS (https://doi.org/10.5281/zenodo.3362844). LiTS2017 is a dataset of 131 contrast-enhanced abdominal CT scans with preoperative tumor localization and postoperative anatomical information, offering 3D masks of the liver and tumor, drawn by radiologists layer by layer, as a gold standard. The CHAOS dataset provides T2-weighted MRI sequences of 40 healthy volunteers and patients, with high-quality annotations for organ segmentation, which were used as additional information for soft-tissue contrast and to test the robustness of cross-modal registration. Both datasets were de-identified. Partial examples of original CT/MRI images for stent design are shown in Figure 4, including preoperative CT scans and post-segmentation images.

The raw data were all converted to NIfTI format and then resampled using trilinear interpolation to an isotropic resolution of 1.0 mm^3. The non-uniformity of the MRI image intensity was corrected using the N4 algorithm, and the gray levels were then normalized linearly. Affine registration was applied to the CT and MRI data at the same time point to ensure rigorous spatial alignment of anatomical structures across modalities, following the principle of maximizing mutual information. The dataset was randomly split into training, validation, and test sets with a 7:1.5:1.5 ratio, using a fixed random seed during splitting to guarantee reproducibility. The input to the dual-channel encoder-shared decoder network was also refined by applying random operations: random rotation, flip, and elastic deformation. The batch size was set to 4; the initial learning rate to 0.001; and the Adam optimizer was used for 200 iterations.

In the biomaterials area, GelMA and HA were dissolved in sterile phosphate buffer at an optimized mass ratio, and a photoinitiator was added to form a bio-ink composite. Rheological analysis demonstrated that the oscillation time scanning revealed a recovery rate of 92% in energy storage modulus after three consecutive strain loading-recovery cycles, indicating that the bio-ink exhibited excellent structural recoverability and printing stability. The composite material exhibited shear-thinning behavior and steady-state viscoelastic characteristics. A DLP-printing unit produced layer-by-layer projection patterns according to the scaffold 3D model, controlling layer thickness at 50 μm and the exposure-time matrix. The cast scaffold was rinsed with phosphate-buffered saline to elute unreacted monomers. The *in vitro* experiment was performed, and fetal bovine serum (FBS) concentrations of 2%, 5%, 10%, and 15% were used for a 7-day culture of the human hepatocellular carcinoma cell line (HepG2). All statistical tests involving multiple group comparisons were performed with Bonferroni correction to control for family error rate.

To guarantee rigor evaluation, five popular benchmark methods were chosen in comparative studies. In the image reconstruction stage, convolutional networks for biomedical image segmentation (U-Net), fully convolutional neural networks for volumetric medical image segmentation (V-Net), and Graph Cut were introduced as references for segmentation performance. For the materials, mechanics, and biology evaluation, four common scaffold types—pure GelMA, polycaprolactone (PCL), poly(lactic-co-glycolic acid) (PLGA), and decellularized extracellular matrix (dECM)—were selected as controls. All comparison methods were run independently three times under the same test set and experimental conditions, and the mean and standard deviation were recorded to eliminate random error. Key parameters for personalized liver scaffold fabrication are shown in Table 1.

3.2. Model training process and segmentation performance evaluation

During model training, the current weight parameters were saved after each iteration, and forward inference calculations were performed on an independent validation dataset. Based on the voxel-level correspondence between the predicted 3D probability map and the manually labeled mask, the volume of the intersection and union region was calculated on a voxel-by-voxel basis to calculate the Dice loss and Dice coefficient. Boundary accuracy was evaluated by extracting the surface point sets from the predicted results and the ground-truth mask, constructing a nearest-neighbor distance matrix, and computing the 95th percentile distance as the Hausdorff distance 95th percentile (HD95) metric. All metrics were computed example-by-example on the complete validation set, and the average is used to produce the single-round evaluation result. The values of the loss function and the three accuracy metrics after each training round were recorded in order, and a continuous performance variation curve was drawn to analyze the evolution of model convergence and spatial segmentation consistency.

As shown in Figure 5, the training epoch is the horizontal coordinate, and the vertical coordinates are the Dice loss, the distance to the Dice coefficient, and the HD95 boundary, respectively, describing the model's convergence and the segmentation accuracy trend.

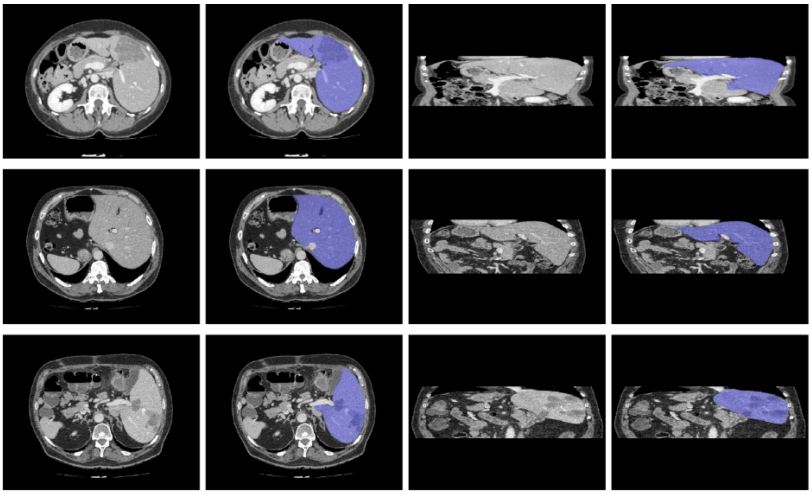

Figure 4. Examples of original computed tomography/magnetic resonance imaging images

Table 1. Key parameters for personalized liver scaffold fabrication

Parameter	Value	Description
CT voxel resolution	1 mm^3	Spatial resampling resolution
MRI voxel resolution	1 mm^3	Spatial resampling resolution
Convolutional network layers	5	Number of encoder layers
Convolution kernel size	3 × 3 × 3	3D convolution kernel dimensions
Dice loss convergence threshold	0.001	Training stop criterion
DLP printing wavelength	405 nm	Ultraviolet light exposure wavelength
Printing layer thickness	50 μm	Thickness of each cured layer
Pore size range	300–500 μm	Internal scaffold pore diameter
GelMA concentration	8%	Volume fraction in bio-ink
HA concentration	2%	Volume fraction in bio-ink
Photoinitiator concentration	0.5% w/v	Concentration of polymerization initiator
PBS crosslinking time	12 h	Scaffold post-processing crosslinking duration

Abbreviations: 3D: Three-dimensional; CT: Computed tomography; DLP: Digital light processing; GelMA: Gelatin methacryloyl; HA: Hyaluronic acid; MRI: Magnetic resonance imaging; PBS: Phosphate-buffered saline.

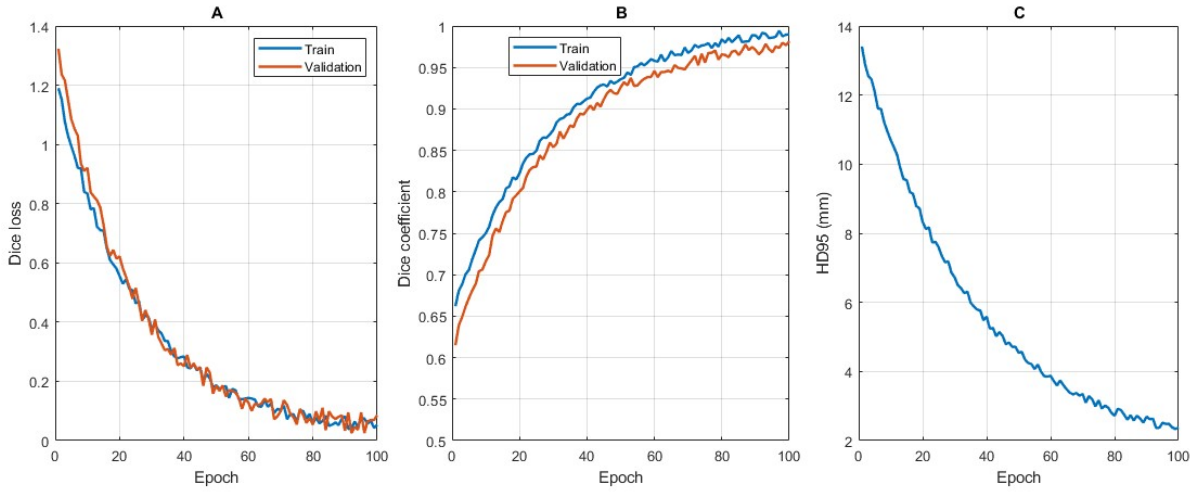

Figure 5. Training convergence and segmentation performance. (A) Training and validation loss. (B) Segmentation accuracy. (C) Boundary distance reduction.

Figure 5A shows that the Dice loss on the training set decreased over time from about 1.2 to about 0.03, and the Dice loss on the validation set also decreased from about 1.32 to about 0.05. The initial descent has a steeper slope, proceeding to flatten out. The trend of exponential decay means that, iteratively, the network rapidly completes low-level feature alignment and rough structure localization in the first stages, while reducing the amplitude of the parameter updates in the second half, and the loss function converges to a stable region. The training and validation curves are close and exhibit small fluctuations, indicating that the network's generalization ability does not change significantly during multimodal feature fusion and that the weight update directions for a considerable portion of the input samples are consistent.

As shown in Figure 5B, the Dice coefficient increased from about 0.67 to nearly 1, while the validation Dice coefficient increased from about 0.62 to about 0.98. The form of the curve followed the trend of loss. The value rapidly rose above 0.9 in the medium term, indicating that integrating features into the shared decoding layer can significantly improve the ability to recognize boundary areas. Then, a deceleration in the rising trend implies that the model has learned most of the information the data contain, and errors are mostly localized to extremely small edge areas.

In Figure 5C, the value of HD95 decreased dismally from about 13.4 mm to approximately 2.3 mm. The dramatic reduction in boundary distance shows that the model achieved its goal, moving from coarse alignment to an exact fit in localizing in space. The decreased magnitude of the curve's fluctuation in the later period suggests that the anatomical edge's predicted result is likely to be steady. These three indicators both demonstrate the stability and convergence of the training process. Multimodal inputs are complementary in their spatial structure and grayscale contrast, which motivates the joint enhancement of segmentation accuracy and boundary agreement.

3.3. Jacobian distribution assessment of the deformation field

A total prime analysis was applied to the Jacobian determinant calculated from the deformation field to obtain the numerical distribution and its frequency of occurrence in the structure. To observe the distribution of the numerical concentration interval cells and tails, a frequency histogram was constructed. Skewness and kurtosis statistics were calculated over a distribution to assess overall symmetry and spread. To verify the continuity of the spatial mapping, the presence of outliers below or near zero was tested. High- and low-value regions were traced back using spatial coordinate indexing to validate the original displacement-gradient variation patterns on a pattern-by-pattern basis. Based on the above statistical and spatial consistency analysis, the anatomical stability and physical rationality of the deformation estimation were considered.

Figure 6 shows the distribution of local volume change after non-rigid registration. Local volume expansion was indicated by a Jacobian determinant larger than 1; local volume compression was represented by a determinant smaller than 1; while unchanged volume was represented by a determinant equal to 1. The data were largely concentrated around 1, with a small skew towards the >1

region, suggesting that slightly more voxels are undergoing mild expansion and that the residual liver is indeed exhibiting an overall net growth trend. The distribution was unimodal, with a mode near 1, and contained no negative values, implying good continuity of the deformation field without non-physical folding or topological defects, and furthermore, the spatial transformation is reversible.

The frequency decreased gradually beyond 1, implying that the contribution from locally intense expansion regions was limited, while most voxels exhibited mild growth. A few voxels lay within the <1 region, representing a minor shrinkage of the edge region during registration, due to deformation balancing during global alignment. The horizontal span of the distribution indicates the extent of spatial variation in proliferation; a narrow distribution corresponds to a more consistent growth pattern, while a broader distribution indicates greater spatial variation. These results confirm a solid foundation on the scaled local volume expansion ratios for spatial mapping and validate that the deformation estimation fulfills the analytical requirements of numerical stability and anatomical meaningfulness.

3.4. Multimodal image reconstruction accuracy validation

The Dice coefficient and Hausdorff distance were selected as the primary quantitative metrics to evaluate overlap and the maximum surface geometric deviation between segmented regions. The test set included three levels of tumor burden: small, medium, and large. Different tumor-burden states were classified by the maximum tumor diameter on preoperative enhanced CT scan, with three ranges: ≤3 cm, >3 and ≤5 cm, and >5 cm. Each experiment was performed three times independently to obtain statistically robust results. The proposed fusion reconstruction approach was then compared to U-Net, V-Net, and Graph Cut methods head-to-head under the same data conditions. The 3D mask of the liver parenchyma and the postoperative defect region was automatically extracted by the system, and the spatial consistency index was calculated between the prediction model and the gold-standard annotation. The mean and standard deviation of each method at different tumor volumes are recorded, and a multi-dimensional error analysis matrix is constructed to impartially assess the algorithm's boundary capturing strength and its anti-interference capability in the presence of complicated body structures.

Figure 7 presents the results of the accuracy assessment for the multimodal image reconstruction. In Figure 7A and 7B, the x-axis represents the four different segmentation and reconstruction methods, while the y-axis represents the Dice coefficient and the Hausdorff distance, respectively. The proposed fusion reconstruction approach achieved the maximum Dice coefficient (average 0.94–0.96) and the minimum Hausdorff distance (average 2.1 mm–3.0 mm) in all tumor burdens, while also exhibiting the smallest data fluctuation range. This superiority is attributed to the dual-channel encoder simultaneously extracting CT bony-structure features and MRI soft-tissue features, which complement each other and prevent gradient vanishing in regions with fuzzy tumor boundaries in unimodal models. The accuracy and variance of traditional U-Net and Graph Cut algorithms degraded rapidly with increasing tumor burden due to the anatomical deformation induced by large tumors, which violated the linear assumptions implicit in their receptive fields or prior models. In contrast, the fusion method performs spatial alignment of cross-modal features using a shared decoder, while preserving the geometric topology of the defect region. The pattern of the error bars also showed that the proposed method was highly robust under various working conditions. The standard deviation of the three independent runs remained low, indicating that the network parameters converge stably and are not significantly influenced by random initialization or data noise. This confirms its suitability as a preoperative planning tool in complex clinical situations.

3.5. Verification of structural fidelity and mechanical properties of the printed scaffold

The cured scaffold was reconstructed in 3D using high-resolution micro-CT scanning. A point cloud registration technique was employed to register the real scanned data to the original computer aided design model. The total shape fidelity was derived for the evaluation of the accuracy of macroscopic geometric reproduction. The wall thickness of important supporting structures was retrieved, and the deviation interval with respect to the theoretical value was analyzed statistically. Mechanical property tests were performed under compressive load mimicking physiological load. The stress-strain curves were obtained to calculate Young's modulus and the yield strength. The GelMA/HA composite scaffold was the investigated group, while typical materials, including pure GelMA, PCL, PLGA, and dECM scaffolds, were selected as controls. All samples were fabricated using the same printing parameters and post-processing. Independent testing of each group was performed three times to exclude batch effects and ensure statistical comparability of the data.

As demonstrated in Table 2, the GelMA/HA composite scaffold displayed better overall shape fidelity (94.82%) and key structural wall thickness deviation (12.3 μm), which is far higher than pure GelMA and the dECM group. The high fidelity is attributed to the suppression

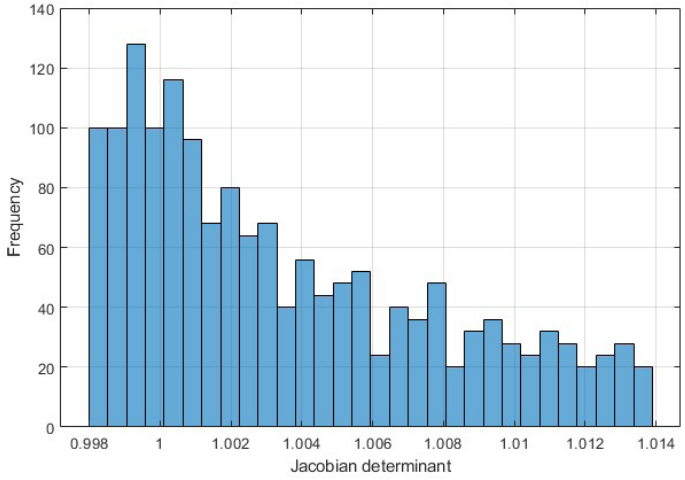

Figure 6. Jacobian distribution of residual liver deformation

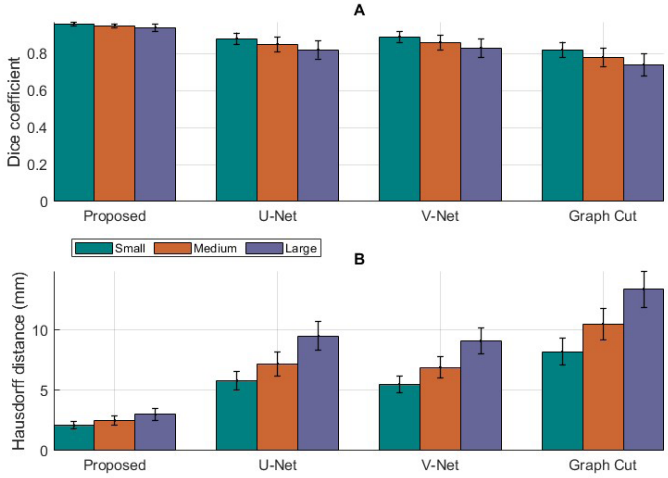

Figure 7. Multimodal image reconstruction accuracy. (A) Segmentation accuract (Dice coefficient). (B) Surface deviation (Hausdorff distance).

Table 2. Comparison of structural fidelity and mechanical properties

Material type	Overall shape fidelity (%)	Wall thickness deviation (μm)	Young's modulus (kPa)	Yield strength (kPa)
GelMA/HA	94.82 ± 0.45	12.3 ± 1.8	48.6 ± 3.2	22.4 ± 1.5
GelMA	88.15 ± 1.23	28.5 ± 4.2	25.3 ± 2.1	11.2 ± 0.9
PCL	96.40 ± 0.30	8.5 ± 1.2	2100.5 ± 150.3	185.6 ± 12.4
PLGA	93.20 ± 0.85	15.6 ± 2.5	1850.2 ± 120.5	160.3 ± 10.8
dECM	82.45 ± 2.10	45.2 ± 6.8	18.5 ± 1.5	8.5 ± 0.7

Abbreviations: dECM: Decellularized extracellular matrix; GelMA: Gelatin methacryloyl; HA: Hyaluronic acid; PCL: Polycaprolactone; PLGA: Poly(lactic-co-glycolic acid).

of photopolymerization shrinkage by the HA nanofiller, which reduces interlayer deformation in DLP printing. Both pure GelMA and dECM are prone to macroscopic geometric collapse and are difficult to maintain complex pore gradients because of their low crosslinking density and water absorption-induced swelling along the microscopic direction, resulting in unpredictable thickening of the wall from inside out. Mechanical tests revealed that the GelMA/HA composite possessed a Young's modulus (48.6 kPa) and a yield strength (22.4 kPa) close to those of physiological normal liver tissue, thereby addressing the drawbacks of pure hydrogels in terms of insufficient mechanical support. Energy dissipation in the HA-induced inorganic–organic interpenetrating network is also a factor. In comparison, PCL and PLGA exhibited extremely high stiffness, with irreversibly two orders of magnitude higher moduli than that of liver tissue, which could induce stress-shielding effects, constraining cellular mechanical signal transduction. The dECM exhibited good mechanical performance and excellent bioactivity, but its low yield strength limited its ability to withstand postoperative intra-abdominal pressure. The GelMA/HA system demonstrated popularity across the geometrical, mechanical, and structural aspects of the physical micro-environment for liver defect repair.

3.6. *In vitro* cell compatibility and proliferative activity assessment

The human hepatocellular carcinoma cell line HepG2 was seeded at a density of 1×10^5 cells/mL on the surface and internal pores of different scaffold materials, placed in Dulbecco's Modified Eagle Medium containing the corresponding FBS concentration, and incubated for seven days in a constant temperature incubator at 37 °C and 5% carbon dioxide. The medium was changed every two days to ensure uniform cell distribution. Four concentrations of FBS—2%, 5%, 10%, and 15%—were employed to mimic variations in the micro-environment from nutrient deprivation to enrichment. The relative cell proliferation rate was measured using the cell counting kit-8 assay to determine the cell number, which represents the alteration of metabolism; simultaneously, dual-color fluorescence staining and confocal microscopy were used to determine the live/dead cell ratio (green indicates live cells, red indicates dead cells), visually describing cell viability. Comparative experiments were performed on the above-mentioned scaffold matrices and on a control at an equal seeding density, with three independent replicates of each sample. The mean and standard deviation were calculated after data acquisition. Two-way analysis of variance (ANOVA) was employed to assess the interaction between material type and serum concentration on stent biocompatibility and to compare stent biocompatibility across microenvironments.

Figure 8A and 8B presents the relative cell proliferation rate and the live/dead cell staining ratio, respectively. The GelMA/HA biphasic scaffold retains the maximum proliferative potential and living cells under all serum concentrations, and especially in low-serum conditions (2% FBS), it has a distinct advantage, in which the relative cell proliferation rate was 0.85 ± 0.04 and live/dead cell staining ratio was 92.5% ± 1.5%, as shown in Figure 9. The incorporation of HA enhanced the surface negative charge density and hydrophilicity, which facilitated serum protein adsorption and integrin-mediated cell adhesion, thus antagonizing the metabolic suppression effects of pure hydrogels under nutrient-limited conditions. PCL and PLGA groups performed poorly because the hydrophobic surface impaired cell spreading and led to elevated contact inhibition and apoptosis, with increasing serum concentration evoking only an insignificant improvement. dECM was comparable to GelMA/HA, but insufficient structural stability in a low-nutrient microenvironment caused cell detachment. Higher serum concentrations generally improved the activity of all groups, indicating that exogenous growth factors drove metabolism. With tailored physicochemical characteristics, the GelMA/HA system provided a stable microenvironment insensitive to serum perturbations, which supported the long-term expansion and maintenance of hepatocyte function in the complex postoperative fluid milieu, demonstrating the feasibility of the material design from a biological perspective.

3.7. In vitro dynamic simulation validation of gradient and personalized design

To decouple the independent contributions of geometric matching and pore gradient to repair efficacy, this study constructed an in vitro dynamic simulation platform based on fluid-structure interaction (FSI). Three control groups were established: (i) non-personalized shape + uniform porosity; (ii) personalized shape + uniform porosity; (iii) personalized shape + gradient porosity (proposed group). All scaffolds were fabricated using the same GelMA/HA material. The scaffolds were placed in an agarose gel matrix simulating the mechanical properties of liver tissue, and periodic physiological loads (simulating respiratory motion and blood flow impact) were applied via a microfluidic pump system. During an 8-week accelerated degradation experiment, changes in scaffold structural integrity were monitored periodically using high-resolution micro-CT scans, and the permeability efficiency of simulated body fluids and nutrient diffusion flux within the scaffolds were quantified using particle image velocimetry (PIV). This

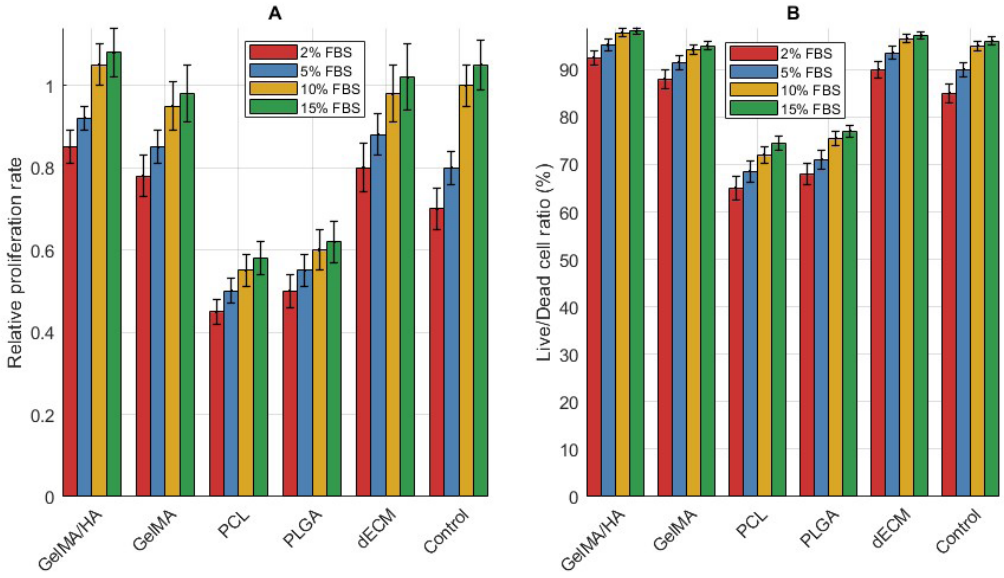

Figure 8. Relative cell proliferation rate and live/dead cell staining ratio. (A) Metabolic activity and proliferation. (B) Cell viability assessment.
Abbreviations: dECM: Decellularized extracellular matrix; FBS: Fetal bovine serum; GelMA: Gelatin methacryloyl; HA: Hyaluronic acid; PCL: Polycaprolactone; PLGA: Poly(lactic-co-glycolic acid).

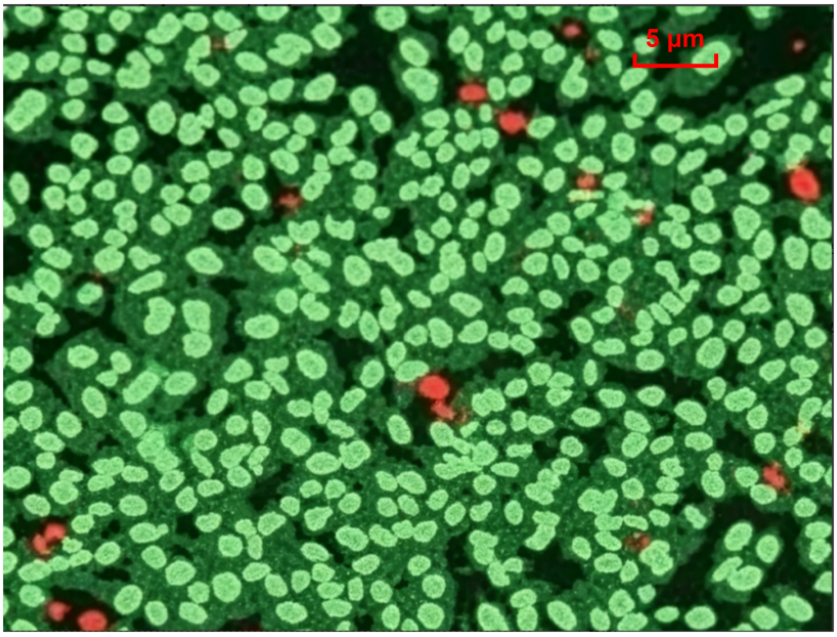

Figure 9. Staining effect under hyposegmentation conditions. Scale bar: 5 μm; magnification: 2,000×.

evaluation aimed to validate the ability of gradient design to maintain structural stability and optimize material transport under dynamic physiological conditions.

Table 3 shows that there are systematic differences in structural integrity retention and effective diffusion coefficient among the three groups of scaffolds. The non-personalized uniform group (A), due to its mismatch between geometry and the defect cavity, is prone to local stress concentration under simulated physiological loads, leading to premature structural collapse and resulting in the lowest integrity retention rate (62.4% ± 3.1%). Its uniform pore structure also limits the diversity of fluid permeation paths, limiting diffusion efficiency (1.85×10^{-6} cm^2/s).

Table 3. Functional validation of gradient and personalized design

Group	Design feature	Structural Integrity Retention (%)	Effective Diffusion Coefficient ($\times 10^{-6}$ cm²/s)
A	Non-personalized + uniform porosity	62.4 ± 3.1	1.85 ± 0.12
B	Personalized + uniform porosity	78.5 ± 2.8	2.40 ± 0.15
C (proposed)	Personalized + gradient porosity	91.2 ± 1.5	3.15 ± 0.18

While the personalized uniform group (B) improved geometric fit and reduced macroscopic deformation, the lack of gradient regulation in the internal pores made it difficult for nutrients to penetrate deep into the core region of the scaffold, resulting in a moderate diffusion coefficient (2.40×10^{-6} cm²/s). In contrast, the personalized gradient group (C) not only fits the shape precisely, but also has porosity that increases from the outside to the inside, forming a channel network that facilitates fluid guidance. While maintaining high structural stability, it significantly optimizes material transport, thus achieving the best integrity retention rate (91.2% ± 1.5%) and diffusion coefficient (3.15×10^{-6} cm²/s).

4. Conclusion

This study developed a personalized repair system for liver cancer resection using multimodal CT/MRI fusion imaging and DLP 3D bioprinting technology. Multi-temporal image registration and deep-learning segmentation algorithms accurately quantified the dynamic regeneration process of residual liver tissue, providing a reliable basis for scaffold geometric design. GelMA/HA composite bio-ink, combined with a gradient-pore-structure optimization strategy, endowed the scaffold with excellent morphological fidelity and mechanical properties that match those of liver tissue. *In vitro* experiments confirmed that the material is cell-compatible, supporting efficient hepatocyte adhesion and proliferation. This study overcame the limitations of traditional static filling, establishing a closed-loop process from imaging diagnosis to physical fabrication, realizing a shift from passive adaptation to active guidance in repair strategies. Future work should focus on integrating vascularized networks and conducting large-scale clinical translational validation to advance precision regenerative medicine.

Acknowledgments

None.

Funding

This work was supported by the Science Research Project of the Education Department of Hunan Province (25C0006, 23B0055).

Conflict of interest

The authors declare they have no competing interests.

Author contributions

Conceptualization: Wen Liu
Formal analysis: Jiaxin Li
Investigation: Yongzhi Chen
Methodology: Yongzhi Chen
Writing–original draft: Ning Zhou
Writing–review & editing: Guanwu Wang

Ethics approval and consent to participate

This study was reviewed and approved by Northern Jiangsu People's Hospital Affiliated to Yangzhou University (Approval ID. yzu-lcyxy-n030).

Consent for publication

Not applicable.

Availability of data

The CT imaging data used in this study were obtained from the LiTS2017 dataset (https://github.com/assassint2017/MICCAI-LITS2017), and the MRI imaging data were obtained from the CHAOS dataset (https://doi.org/10.5281/zenodo.3362844). Both datasets are publicly available for research purposes.

References

1. Primavesi F, Maglione M, Cipriani F, *et al.* E-AHPBA–ESSO–ESSR Innsbruck consensus guidelines for preoperative liver function assessment before hepatectomy. *Br J Surg.* 2023;110(10):1331-1347.

   doi: 10.1093/bjs/znad233

2. Kimura J, Takagi K, Fuji T, *et al.* Risk Factors and Strategies for Failure to Rescue Following Hepatectomy: A Review. *J Hepato Biliary Pancreat Sci.* 2025;32(11):801-809.

   doi: 10.1002/jhbp.70014

3. Birgin E, Abdelhadi S, Seyfried S, *et al.* Robotic or laparoscopic repeat hepatectomy after open hepatectomy: a cohort study. *Surg Endosc.* 2024;38(3):1296-1305.

   doi: 10.1007/s00464-023-10645-2

4. Raptis DA, Elsheikh Y, Alnemary Y, *et al.* Robotic living donor hepatectomy is associated with superior outcomes for both the donor and the recipient compared with laparoscopic or open-A single-center prospective registry study of 3448 cases. *Am J Transplant.* 2024;24(11):2080-2091.

   doi: 10.1016/j.ajt.2024.04.020

5. Broering DC, Raptis DA, Elsheikh Y. Pioneering fully robotic donor hepatectomy and robotic recipient liver graft implantation–a new horizon in liver transplantation. *Int J Surg.* 2024;110(3):1333-1336.

   doi: 10.1097/JS9.0000000000001031

6. Wong P, Vien P, Kessler J, *et al.* Augmenting the future liver remnant prior to major hepatectomy: a review of options on the menu. *Ann Surg Oncol.* 2025;32(8):5694-5709.

   doi: 10.1245/s10434-025-17607-z

7. Mao B, Zhu S, Li D, *et al.* Comparison of safety and effectiveness between robotic and laparoscopic major hepatectomy: a systematic review and meta-analysis. *Int J Surg.* 2023;109(12):4333-4346.

   doi: 10.1097/JS9.0000000000000750

8. Berardi G, Cucchetti A, Colasanti M, *et al.* Prehabilitation with exercise and nutrition to reduce morbidity of major hepatectomy in patients with sarcopenia: the PREHEP randomized clinical trial. JAMA surgery, 2025, 160(10): 1068-1075.

   doi: 10.1001/jamasurg.2025.3102

9. Hong SK, Kim J Y, Lee J, *et al.* Pure laparoscopic donor hepatectomy: experience of 556 cases at Seoul National University Hospital. *Am J Transplant.* 2024;24(2):222-238.

   doi: 10.1016/j.ajt.2023.06.007

10. Zhu XD, Huang C, Shen YH, *et al.* Hepatectomy after conversion therapy using tyrosine kinase inhibitors plus anti-PD-1 antibody therapy for patients with unresectable hepatocellular carcinoma. *Ann Surg Oncol.* 2023;30(5):2782-2790.

    doi: 10.1245/s10434-022-12530-z

11. Cheah YL, Yang HY, Simon CJ, *et al.* The learning curve for robotic living donor right hepatectomy: Analysis of outcomes in 2 specialized centers. *Liver Transplant.* 2025;31(2):190-200.

    doi: 10.1097/LVT.0000000000000480

12. Sun M, Li M, Hu M, *et al.* Fully bioactive nanodrugs: stem cell-derived exosomes engineered with biomacromolecules to treat CCl4-and extreme hepatectomy-induced acute liver failure. *ACS Nano.* 2024;18(50):33907-33921.

    doi: 10.1021/acsnano.4c07408

13. Yang DL, Peng N, Nong JL, *et al.* Survival benefit of hepatectomy after complete or partial response to conversion therapy in unresectable hepatocellular carcinoma (GUIDANCE003): a multicenter study. *Liver Cancer.* 2025;14(6):687-703.

    doi: 10.1159/000546052

14. Cusumano C, Kansoun A, Tougoue FK, *et al.* Incidence and outcomes of post-hepatectomy diaphragmatic hernia: a systematic review. *HPB.* 2023;25(12):1466-1474.

    doi: 10.1016/j.hpb.2023.08.008

15. Liu Y, Wang Q, Du B, *et al.* A meta-analysis of the three-dimensional reconstruction visualization technology for hepatectomy. *Asian J Surg.* 2023;46(2):669-676.

    doi: 10.1016/j.asjsur.2022.07.006

16. Sambommatsu Y, Kumaran V, Imai D, *et al.* Early outcomes of robotic vs open living donor right hepatectomy in a US Center. *Surg Endosc.* 2025;39(3):1643-1652.

    doi: 10.1007/s00464-024-11469-4

17. Zhang XP, Zhang TC, Wu FF, *et al.* Patterns and outcomes of early and late recurrence after hepatectomy for hepatocellular carcinoma with microvascular invasion: a multicenter study in China. *Hepatol Int.* 2025;19(4):903-914.

    doi: 10.1007/s12072-025-10802-w

18. Zhang Y, Li L, Dong L, *et al.* Hydrogel-based strategies for liver tissue engineering. *Chem Bio Eng.* 2024;1(11):887-915.

    doi: 10.1021/cbe.4c00079

19. Du Y, Bai Y, Lang S, *et al.* Gelatin sponges with a uniform interoperable pore structure and biodegradability for liver injury hemostasis and tissue regeneration. *Biomacromolecules.* 2023;24(11):5313-5327.

    doi: 10.1021/acs.biomac.3c00803

20. Farasati Far B, Isfahani AA, Nasiriyan E, *et al.* An updated review on advances in hydrogel-based nanoparticles for liver cancer treatment. *Livers.* 2023;3(2):161-189.

    doi: 10.3390/livers3020012

21. Mukherjee P, Guha S, Ghosh A, *et al.* Porous Organic Polymer-Based Nanocomposites for Hypoxia Relieving and Enhanced Chemotherapy in Hepatocellular Carcinoma. *ACS Appl Bio Mater.* 2024;7(9):6138-6151.

    doi: 10.1021/acsabm.4c00723

22. Caruso D, De Santis D, Del Gaudio A, *et al.* Low-dose liver CT: image quality and diagnostic accuracy of deep learning image reconstruction algorithm. *Eur Radiol.* 2024;34(4):2384-2393.

    doi: 10.1007/s00330-023-10171-8

23. Wu T, Yang D, Wee A, *et al.* Identification of MRI features associated with injury type, severity, and prognosis in drug-induced liver injury. *Eur Radiol.* 2023;33(1):666-677.

    doi: 10.1007/s00330-022-09041-6

24. Jeong B, Heo S, Lee SS, *et al.* Predicting post-hepatectomy liver failure in patients with hepatocellular carcinoma: nomograms based on deep learning analysis of gadoxetic acid-enhanced MRI. *Eur Radiol.* 2025;35(5):2769-2782.

doi: 10.1007/s00330-024-11173-w

25. Görgec B, Hansen IS, Kemmerich G, *et al.* MRI in addition to CT in patients scheduled for local therapy of colorectal liver metastases (CAMINO): an international, multicentre, prospective, diagnostic accuracy trial. *Lancet Oncol.* 2024;25(1):137-146.

doi: 10.1016/S1470-2045(23)00572-7

26. Cha H, Choi JY, Park YN, *et al.* Comparison of imaging findings of macrotrabecular-massive hepatocellular carcinoma using CT and gadoxetic acid–enhanced MRI. *Eur Radiol.* 2023;33(2):1364-1377.

doi: 10.1007/s00330-022-09105-7

27. Pei C, Wu F, Yang M, *et al.* Multi-source domain adaptation for medical image segmentation. *IEEE Trans Med Imaging* 2023;43(4):1640-1651.

doi: 10.1109/TMI.2023.3346285

28. Odisio BC, Albuquerque J, Lin YM, *et al.* Software-based versus visual assessment of the minimal ablative margin in patients with liver tumours undergoing percutaneous thermal ablation (COVER-ALL): a randomised phase 2 trial. *Lancet Gastroenterol Hepatol.* 2025;10(5):442-451.

doi: 10.1016/S2468-1253(25)00024-X

29. Wu Y, Su H, Li M, *et al.* Digital light processing-based multi-material bioprinting: Processes, applications, and perspectives. *J Biomed Mater Res Part A.* 2023;111(4):527-542.

doi: 10.1002/jbm.a.37473

30. Dhand AP, Davidson MD, Burdick JA. Lithography-based 3D printing of hydrogels. *Nat Rev Bioeng.* 2025;3(2):108-125.

doi: 10.1038/s44222-024-00251-9

31. Gadre M, Vasanthan KS. Engineering a GelMA–dECM-based 3D bioprinted liver fibrosis model: methotrexate-induced functional and molecular validation. *RSC Adv.* 2025;15(44):37012-37026.

doi: 10.1039/D5RA05955K

32. Shinn J, Park S, Lee S, *et al.* Antioxidative hyaluronic acid–bilirubin nanomedicine targeting activated hepatic stellate cells for anti-hepatic-fibrosis therapy. *ACS Nano.* 2024;18(6):4704-4716.

doi: 10.1021/acsnano.3c06107

33. Xiao L, Ye M, Fan Y, *et al.* Dual-cross-linked methylacrylated collagen-DPPA bioinks for precision dlp bioprinting and accelerated skin wound healing. *Biomacromolecules.* 2025;26(7):4308-4321.

doi: 10.1021/acs.biomac.5c00305

34. Kim MH, Lin CC. Poly (ethylene glycol)–norbornene as a photoclick bioink for digital light processing 3D bioprinting. *ACS Appl Mater Interfaces.* 2023;5(2):2737-2746.

doi: 10.1021/acsami.2c20098

35. Kim D H, Byun J Y, Kim D, *et al.* Geometric evaluation of biomimetic 3D printed rat femur. *J Hard Tissue Biol.* 2023;32(2):133-138.

doi: 10.2485/jhtb.32.133

36. Wang K, Wang J, Jiang P. High-dose-rate three-dimensional image-guided adaptive brachytherapy (3D IGABT) for locally advanced cervical cancer (LACC): A narrative review on imaging modality and clinical evidence. *Curr Oncol.* 2023;31(1):50-65.

doi: 10.3390/curroncol31010004

37. Ding H, Chen L, Tao Q, *et al.* DCU-Net: a dual-channel U-shaped network for image splicing forgery detection. *Neural Comput Appl.* 2023;35(7):5015-5031.

doi: 10.1007/s00521-021-06329-4

38. Li M, Zhang W, Hu B, *et al.* Automatic assessment of depression and anxiety through encoding pupil-wave from HCI in VR scenes. *ACM Trans Multimed Comput Commun Appl.* 2023;20(2):1-22.

doi: 10.1145/3513263